

Assessment of Surface Exchange Coefficients in the Noah-MP Land Surface Model for Different Land Cover Types over China

Xia Zhang¹, Liang Chen¹, Zhuguo Ma¹, and Yanhong Gao²

¹Key Laboratory of Regional Climate–Environment Research for Temperate East Asia, Institute of Atmospheric Physics, Chinese Academy of Sciences, Beijing, China

²Key Laboratory of Land Surface Process and Climate Change in Cold and Arid Regions, Northwest Institute of Eco-Environment and Resources, Chinese Academy of Sciences, Lanzhou, China

November 23, 2022

Abstract

The parameterization of surface exchange coefficients (Ch) representing land–atmosphere coupling strength plays a key role in land surface modeling. Previous studies have found that land–atmosphere coupling in land surface models (LSMs) is overestimated, which affects the predictability of weather and climate evolution. To improve the representation of land–atmosphere interactions in LSMs, this study investigated the dynamic canopy-height-dependent coupling strength in the offline Noah LSM with multiparameterization options (Noah-MP) when applied to China. Comparison with the default Noah-MP LSM showed the dynamic scheme significantly improved the Ch calculations and realistically reduced the biases of simulated surface energy and water components against observations. It is noteworthy that the improvements brought by the dynamic scheme differed across land cover types. The scheme was found superior in reproducing the observed Ch as well as surface energy and water variables for short vegetation (grass, crop, and shrub), while the improvement for tall canopy (forest) was found not significant, although the estimations were reasonable. The improved version benefits from the treatment of the roughness length for heat. Overall, the dynamic coupling scheme markedly affects the simulation of land–atmosphere interactions, and altering the dynamics of surface coupling has potential for improving the representation of land–atmosphere interactions and thus furthering LSM development.

1 **Assessment of Surface Exchange Coefficients in the Noah-MP Land**
2 **Surface Model for Different Land Cover Types over China**

3
4 **Xia Zhang^{1,2}, Liang Chen^{1,*}, Zhuguo Ma^{1,2}, and Yanhong Gao³**

5 ¹Key Laboratory of Regional Climate–Environment Research for Temperate East
6 Asia, Institute of Atmospheric Physics, Chinese Academy of Sciences, Beijing, China,

7 ²University of Chinese Academy of Sciences, Beijing, China,

8 ³Key Laboratory of Land Surface Process and Climate Change in Cold and Arid
9 Regions, Northwest Institute of Eco-Environment and Resources, Chinese Academy of
10 Sciences, Lanzhou, China

11 *Corresponding author: Liang Chen (chenliang@tea.ac.cn)

12
13
14
15
16
17 **Key Points:**

- 18 • Impacts of C_{zil} on coupling strength as well as surface energy and water
19 components over China were simulated
- 20 • The dynamic canopy-height-dependent C_{zil} scheme was found superior in
21 reproducing observations
- 22 • The dynamic scheme performed better for short vegetation because of the
23 treatment of the roughness length for heat

28 **Abstract**

29 The parameterization of surface exchange coefficients (C_h) representing land–
30 atmosphere coupling strength plays a key role in land surface modeling. Previous
31 studies have found that land–atmosphere coupling in land surface models (LSMs) is
32 overestimated, which affects the predictability of weather and climate evolution. To
33 improve the representation of land–atmosphere interactions in LSMs, this study
34 investigated the dynamic canopy-height-dependent coupling strength in the offline
35 Noah LSM with multiparameterization options (Noah-MP) when applied to China.
36 Comparison with the default Noah-MP LSM showed the dynamic scheme
37 significantly improved the C_h calculations and realistically reduced the biases of
38 simulated surface energy and water components against observations. It is noteworthy
39 that the improvements brought by the dynamic scheme differed across land cover
40 types. The scheme was found superior in reproducing the observed C_h as well as
41 surface energy and water variables for short vegetation (grass, crop, and shrub), while
42 the improvement for tall canopy (forest) was found not significant, although the
43 estimations were reasonable. The improved version benefits from the treatment of the
44 roughness length for heat. Overall, the dynamic coupling scheme markedly affects the
45 simulation of land–atmosphere interactions, and altering the dynamics of surface
46 coupling has potential for improving the representation of land–atmosphere
47 interactions and thus furthering LSM development.

48 **Keywords:** land–atmosphere interaction; surface coupling strength; surface exchange
49 coefficient; surface fluxes

50

51

52

53

54 **1. Introduction**

55 Land–atmosphere interactions that are manifest as the exchange of energy, mass, and
56 momentum between the land surface and the atmosphere play a fundamental role in
57 the evolution of weather and climate systems (Betts et al., 1996; Knist et al., 2017;
58 Los et al., 2006; Mahmood & Hubbard, 2003). Recent studies have shown that
59 excessive land–atmosphere coupling in numerical models leads to large uncertainties
60 regarding surface energy and water components. For example, Koster et al. (2004)
61 identified several “hot spots” in terms of strong coupling between soil moisture (SM)
62 and rainfall, some of which could not be captured correctly in the Global Land–
63 Atmosphere Coupling Experiment study (Dirmeyer et al., 2006) or even did not
64 register as regions of strong land–atmosphere coupling, e.g., the U.S. Southern Great
65 Plains (Zhang et al., 2008). Relevant studies have been restricted by many factors
66 such as the treatment of the roughness length for heat in land surface
67 parameterizations (Chen et al., 1997; Chen & Zhang, 2009; LeMone et al., 2008) and
68 the accuracy of the meteorological inputs (Santanello et al., 2009). Such work has
69 highlighted the critical importance of models in predicting the strength of land–
70 atmosphere coupling, as expressed by the surface exchange coefficients (C_h), although
71 such fundamental coupling remains poorly understood.

72 The efficiencies of the exchange of energy and water vapor between the land surface
73 and the lower atmosphere are represented by the parameter C_h . In a land surface
74 model (LSM), this parameter controls the land–atmosphere coupling strength for
75 different land cover types and climate regimes (Garratt, 1992; LeMone et al., 2008),
76 which has consequences regarding the prediction of atmospheric, hydrological, and
77 ecological components (LeMone et al., 2008; Li et al., 2009; Yang et al., 2011). The
78 Noah LSM with multiparameterization options (Noah-MP) is a state-of-the-art LSM
79 (Niu et al., 2011; Yang et al., 2011) that is used as an augmented land–surface scheme
80 for the atmospheric Weather Research and Forecasting model (Burlage et al., 2015;
81 Skamarock et al., 2008). Two C_h calculations provided in the Noah-MP LSM are the

82 Monin–Obukhov (M-O) (Brutsaert, 1982) and Chen97 (Chen et al., 1997) schemes,
83 both of which are obtained through the M-O similarity theory and are mainly
84 dependent on the roughness length for heat or moisture (Z_{ot}) and momentum (Z_{om}) as
85 well as the atmospheric stability. The Chen97 scheme accounts for the difference
86 between Z_{ot} and Z_{om} but not for zero-displacement height, while the M-O scheme is
87 the opposite. The differences lead to the M-O scheme theoretically producing greater
88 C_h and hence larger sensible heat flux (SH) than Chen97 (Niu et al., 2011). Recently,
89 studies have indicated some deficiencies of the two schemes in their representation of
90 land surface processes. For example, the M-O scheme stimulates more runoff than the
91 Chen97 scheme, which is more consistent with observations (Yang et al., 2011).
92 Moreover, Pilotto et al. (2015) found that using the M-O scheme produces surface
93 fluxes and runoff with significant errors for an Amazonia forest site. However, the
94 M-O scheme markedly improves the simulation of the land skin temperature, while
95 Chen97 shows significant cold bias in arid regions of the western U.S. (Niu et al.,
96 2011). The discrepancies are mainly attributed to the treatment of Z_{ot}/Z_{om} (Chen et al.,
97 1997; Chen & Zhang, 2009). The parameter Z_{ot} is different from Z_{om} because heat and
98 momentum transfers are determined by different resistances and mechanisms within
99 the roughness layer (Chen & Zhang, 2009; Sun & Mahrt, 1995). The Z_{ot}/Z_{om} ratio can
100 modulate surface fluxes through the change of an empirical coefficient C_{zil}
101 (Zilitinkevich, 1995). Although the Chen97 scheme considers the differences between
102 Z_{ot} and Z_{om} , a constant C_{zil} (usually specified as 0.1) is adopted in the C_h calculation of
103 the scheme. However, studies have shown that C_{zil} values are dependent on vegetation
104 type and that a dynamic C_{zil} could be more appropriate for reducing the impact of
105 land–atmosphere coupling strength on surface fluxes (Chen & Zhang, 2009; Zheng et
106 al., 2015). These earlier studies have shown the great potential for improvement in
107 model performance through implementation of a dynamic C_{zil} in the M-O scheme that
108 accounts for zero-displacement height, which is not considered in the Chen97 scheme
109 (Yang et al., 2011).

110 Chen et al. (2019) assessed the effect of a dynamic C_{zil} on surface heat flux,
 111 temperature, and precipitation at eight FLUXNET Canada sites and seven AmeriFlux
 112 sites. However, the impact of land–atmosphere coupling within LSMs with regard to
 113 China has yet to be clarified because of the complexity of climate change, terrain, and
 114 vegetation distribution as well as the lack of observations. In the current study, we
 115 extended that modeling and analysis method using data collected from nine ChinaFlux
 116 sites and obtained from the China Meteorological Administration. Using the offline
 117 Noah-MP LSM, the objective of this study is to evaluate the impact of C_{zil} in the M-O
 118 scheme on land–atmosphere coupling strength as well as on surface energy and water
 119 components over China. Section 2 describes the experimental setup of the offline
 120 Noah-MP LSM and provides details of the land–atmosphere coupling method. Section
 121 3 focuses on evaluation of the simulation results against observations in terms of
 122 coupling strength as well as surface energy and water components. Discussions and
 123 conclusions are provided in sections 4 and 5, respectively.

124 **2. Data and Methods**

125 **2.1. Land–Atmosphere Coupling Method**

126 LSMs can provide SH and surface latent heat flux (LH), as lower-boundary-layer
 127 conditions for coupled atmospheric models, to control the diurnal evolution and
 128 stability of the planetary boundary layer and subsequently to affect the development
 129 of weather and climate (Liu et al., 2017; Trier et al., 2011). SH and LH are determined
 130 through the bulk transfer relations (Garratt, 1992) as:

$$131 \quad SH = \rho C_p C_h |U| (\theta_s - \theta_a) \quad (1)$$

$$132 \quad LH = \rho C_e |U| (q_s - q_a) \quad (2)$$

$$133 \quad C_h = \frac{SH}{\rho C_p |U| (\theta_s - \theta_a)} \quad (3)$$

134 where ρ is the air density, C_p is the heat capacity of air, and U is the wind speed. Here,
 135 C_h and C_e are the surface exchange coefficients of SH and LH , respectively.
 136 Generally, C_e is assumed equal to C_h , which controls the total surface heat flux input

137 into the atmosphere and can be associated directly with the coupling strength;
 138 therefore, we hereafter focus on C_h . In the above equations, θ_a and q_a represent the
 139 potential temperature and specific humidity of the air at the lowest model level or at a
 140 specific measurement height above the ground, and θ_s and q_s are the surface potential
 141 temperature and specific humidity. In addition, the observed C_h can be reconstituted
 142 from the observations of variables contained in Eq. (3) transformed from Eq. (1)
 143 (Chen & Zhang, 2009). Instruments at observing stations can provide direct
 144 measurements of SH and U , whereas θ_a is calculated from observed air temperature
 145 adjusted adiabatically for height above the surface, and θ_s is converted from downward
 146 and upward longwave radiation with the surface emissivity derived from observations
 147 (Yang et al., 2008). The values of C_p and ρ are derived from air temperature, relative
 148 humidity, and precipitation.

149 Within the Noah-MP LSM, C_h for the M-O scheme is computed based on the M-O
 150 similarity theory (Brutsaert, 1982) as:

$$151 \quad C_h = \frac{k^2}{\left[\ln\left(\frac{z-d_0}{z_{om}}\right) - \psi_m\left(\frac{z-d_0}{L}\right) \right] \left[\ln\left(\frac{z-d_0}{z_{ot}}\right) - \psi_h\left(\frac{z-d_0}{L}\right) \right]} \quad (4)$$

152 where L is the M-O length, k is the von Kármán constant ($=0.4$), d_0 is the
 153 zero-displacement height, Ψ_m and Ψ_h are stability functions, Z is the height above the
 154 ground surface, Z_{om} is the roughness length for momentum, and Z_{ot} is the roughness
 155 length for moisture and heat. The parameter Z_{om} represents the height at which the
 156 average wind goes to zero and the scalars at $Z < Z_{om}$ are assumed transported by
 157 molecular processes. The parameter Z_{ot} is the height at which the air temperature is
 158 equal to the soil surface temperature.

159 In the Noah-MP LSM, Z_{ot} is related to Z_{om} as a function of atmospheric flow, as
 160 proposed by Zilitinkevich (1995):

$$161 \quad Z_{ot} = Z_{om} \exp(-kC_{zil}\sqrt{R_e}), \quad R_e = \frac{u_0^* Z_{om}}{\nu} \quad (5)$$

162 where C_{zil} is an empirical coefficient, R_e is the roughness Reynolds number, u_0^* is the
 163 friction velocity, and ν is the kinematic molecular viscosity. The C_{zil} values are

164 assumed to vary from 0.01 to 1.00, denoting strong to weak surface coupling (Chen et
165 al., 1997; Zheng et al., 2015). The value of C_{zil} is usually specified as 0.1, which is
166 based on calibration with field data measured over grassland (Chen et al., 1997).

167 Smaller values of C_{zil} generate larger Z_{ot} , which indicates a rougher surface for heat
168 and moisture, resulting in stronger turbulence and larger C_h . The adjustment of C_{zil}
169 can contribute to improved model estimates of surface fluxes (Gutmann & Small,
170 2007; LeMone et al., 2008; Moncrieff, 2004). Furthermore, using the least squares
171 regression method, Chen and Zhang (2009) analyzed multiyear Ameriflux data to
172 determine that C_{zil} values are dependent on vegetation type and can be represented as
173 a function of canopy height h (unit: m):

$$174 \quad C_{zil} = 10^{(-0.4h)} \quad (6)$$

175 The primary focus of this study was implementation of the formula for the
176 canopy-height-dependent C_{zil} into the M-O scheme to assess its impact on the
177 simulations.

178 **2.2. Offline Noah-MP LSM and Modeling Setting**

179 The Noah-MP LSM has been developed to improve the performance of the Noah
180 LSM (Chen & Dudhia, 2001; Chen et al., 1996), and it provides a
181 multiparameterization framework that allows different combinations of available land
182 process schemes (Niu et al., 2011; Yang et al., 2011). In this study, the Noah-MP
183 LSM v3.6 was used in an offline standalone mode to execute single-site and
184 regional-scale land surface experiments. Single-point experiments were executed at
185 nine flux tower sites (Figure 1 and Table 1), while the simulated regional domain
186 covered all of China (Figure 1). The atmospheric forcing fields used in the Noah-MP
187 LSM were wind speed, air temperature, relative humidity, air pressure, precipitation,
188 and downward shortwave and longwave radiation. Single-point experiments were
189 forced by 30-min ChinaFlux observations; regional experiments were forced by the
190 Global Land Data Assimilation System (GLDAS2.1) product with temporal and
191 spatial resolutions of 3 h and 0.25° , respectively, during 2003–2012 (Rodell et al.,

192 2004). Regional simulations were initialized using the land use, soil texture, terrain
193 height, and land–water mask through the preprocessing system of the Weather
194 Research and Forecasting model. The Noah-MP physics options used in the study are
195 listed in Table 2.

196 Three cases were designed to simulate the different responses of coupling strength as
197 well as the surface water and energy components to C_{zil} in the M-O scheme: (1) the
198 original M-O option with identical Z_{om} and Z_{ot} (Default), (2) a constant C_{zil} specified
199 as 0.1 ($C_{zil} = 0.1$ or Czil), and (3) a dynamic canopy-height-dependent C_{zil} (C_{zil-h} or
200 Newczil). In these simulations, everything was identical except for the surface-layer
201 parameterization scheme.

202 To initialize the Noah-MP LSM properly, we first examined the spin-up time required
203 to reach the equilibrium stage, defined as when the difference between two
204 consecutive one-year simulations becomes $<0.1\%$ for the annual means (Cai et al.,
205 2014; Chen et al., 2016; Yang et al., 1995). Almost all sites required no more than 9
206 years to reach equilibrium, except site Sw2 (at least 13 years). Areas with sparse
207 vegetation and deep soil layers usually require a long time to reach equilibrium, which
208 was true of Sw2 being the driest of the nine sites (Chen & Mitchell, 1999; Cosgrove et
209 al., 2003). Consequently, we ran a 10-year spin-up initialization for all stations except
210 Sw2 (20 years) for the single-point experiments, and we conducted 20-year-long runs
211 as spin-up for the regional experiments.

212 **2.3. Validation Datasets**

213 The ChinaFlux network provides observations at 30-min intervals at nine flux tower
214 sites located in areas with different land cover types (grassland, forest, and wetland)
215 and climatic regimes (arid, wet, semiarid, and semihumid regions). Figure 1 shows the
216 geographical locations of the nine ChinaFlux network sites and associated general
217 information is presented in Table 1. Surface energy and water variables in the
218 observations were used for evaluation of the LSM outputs in addition to forcing the
219 Noah-MP single-point experiments. Several missing data for relative humidity and net

220 surface radiation were gap-filled using the nearby observations.
 221 Regional C_h was calculated using surface monthly meteorological data (V3.0) obtained
 222 from the China Meteorological Administration. These data comprised monthly air
 223 temperature, wind speed, relative humidity, pressure, and ground surface temperature
 224 obtained at over 2000 stations during 2003–2012. We interpolated these monthly site
 225 observations to 0.25° spatial resolution using a Cressman-type interpolation.
 226 Regional-scale surface energy fluxes simulated by the Noah-MP LSM were validated
 227 using observation-based FLUXNET-MTE (Model Tree Ensemble) data. The gridded
 228 FLUXNET-MTE dataset, with monthly temporal resolution and 0.0833° spatial
 229 resolution, was integrated with observations from global 253 FLUXNET eddy
 230 covariance towers using machine learning technology, i.e., the MTE algorithm (Jung et
 231 al., 2009). We resampled the products from 0.0833° to 0.25° using a bilinear
 232 interpolation method. The gridded dataset was incomplete over western China because
 233 of the lack of in situ observations. Moreover, the uncertainty in the FLUXNET-MTE
 234 product owing to the uneven spatial distribution of flux towers selected for training the
 235 model tree is not negligible.

236 **2.4. Evaluation Statistics**

237 The level of agreement between model simulations and field observations is usually
 238 measured via three statistics (Brovkin et al., 2013; Dai et al., 2019;
 239 Frydrychowicz-Jastrzebska & Bugala, 2015): the Pearson correlation coefficient (R),
 240 root mean square error (RMSE), and mean bias error (MBE):

$$241 \quad R = \frac{\sum_{i=1}^N (M_i - \bar{M}) (O_i - \bar{O})}{\sqrt{\sum_{i=1}^N (M_i - \bar{M})^2} \sqrt{\sum_{i=1}^N (O_i - \bar{O})^2}} \quad (7)$$

$$242 \quad \text{MBE} = \frac{1}{N} \sum_{i=1}^N (M_i - O_i) \quad (8)$$

$$243 \quad \text{RMSE} = \sqrt{\frac{\sum_{i=1}^N (M_i - O_i)^2}{N}} \quad (9)$$

244 where M_i and O_i are the model simulated and field observed values for the same
245 variable, respectively, \bar{M} and \bar{O} are the means of the simulations and observations,
246 respectively, and N is the number of days.

247 **3. Model Verification and Comparisons**

248 To explore the sensitivity of land–atmosphere coupling strength to C_{zil} , and to
249 determine whether the C_{zil} - h scheme could improve climate simulations, three C_{zil}
250 schemes (the default M-O, $C_{zil} = 0.1$, and C_{zil} - h) were implemented in the Noah-MP
251 LSM and evaluated for different land cover types over China. First, we compared the
252 performance of each scheme in quantifying the land–atmosphere coupling strength
253 against the observed C_h , and then we assessed the impact on the surface energy and
254 water components.

255 **3.1. Surface Coupling Strength Sensibility to C_{zil}**

256 Because the representation of C_{zil} realized by varying the degrees of surface exchange
257 simulation significantly affects the evolution of weather and climate systems (Chen &
258 Zhang, 2009; LeMone et al., 2008; Trier et al., 2011), we first analyzed the impact of
259 each C_{zil} scheme on its C_h calculation. Figure 2 compares the observations and
260 simulations of the midday C_h averaged from 10:00–15:00 local time for the nine
261 ChinaFlux sites in spring and summer, i.e., during the growth season of vegetation.
262 Compared with the observation-derived C_h , the C_h values modeled by the Noah-MP
263 LSM have much smaller variability and seasonality across the various land cover
264 types. Boreal sites (such as Cng) experience a large increase in summer C_h as the land
265 cover changes from a smooth sparsely vegetated surface in spring to a rougher surface
266 with flourishing vegetation in summer, as reflected clearly by the observed C_h . The
267 simulated C_h values based on the default M-O scheme are substantially overestimated
268 at almost all sites, especially in grassland areas. The C_h values simulated in the $C_{zil} =$
269 0.1 experiment are decreased, but the unsatisfactory reduction results in insufficient
270 underestimation at grassland sites and slightly too efficient underestimation for forest

271 sites. In comparison, the C_h values derived from the C_{zil-h} scheme are in better
272 agreement with the observations, especially sites with short vegetation (such as grass),
273 suggesting significant improvement in the performance of the C_{zil-h} scheme in
274 comparison with the other two in terms of the representation of the land–atmosphere
275 coupling strength. Additionally, the C_{zil-h} scheme provides reasonable estimations,
276 similar to the default M-O scheme, at sites with tall vegetation (such as forest),
277 although the overestimated C_h values against the observations, which are consistent
278 with results over North America (Chen et al., 2019; Chen & Zhang, 2009), indicate
279 similar skill of the C_{zil-h} scheme in terms of global applicability.

280 To confirm the findings obtained from the single-site simulations, long-term regional
281 climate modeling over China was conducted to further examine the climatological
282 behavior of land–atmosphere coupling strength sensibility to C_{zil} . Figure 3 shows the
283 observed and Noah-MP modeled C_h over China during the summers of 2003–2012.
284 Spatial climatology differences between the observations and the simulations of the
285 three C_{zil} schemes are shown in Figure 3a–c. Compared with the observations, the C_h
286 values of the default M-O scheme are substantially overestimated with too efficient
287 coupling, while the $C_{zil} = 0.1$ scheme slightly modulates the positive deviation. In
288 contrast, the C_{zil-h} scheme presents the smallest bias against the observations for short
289 vegetation types (grass, crop, and shrub), and it produces overestimated but
290 reasonable C_h values for sites with tall vegetation (forest) in comparison with the
291 default run, with similar results for the nine ChinaFlux sites. Spatial differences
292 between the C_{zil} schemes (Figure 3d and 3e) also show that both the $C_{zil} = 0.1$ and the
293 C_{zil-h} schemes present negative bias against the default run in most parts of China.
294 Additionally, the spatial patterns of the differences are similar to that of vegetation
295 canopy height, implied by a significant boundary between short and tall canopy, for
296 either the $C_{zil} = 0.1$ scheme or the C_{zil-h} scheme. These findings indicate that the C_h
297 values are more realistically related to the canopy-height-dependent C_{zil} . From the
298 perspective of vegetation type, we further quantified the sensitivity of the coupling

299 strength response to C_{zil} for different land cover types, as shown in Figure 3f. For
300 barren land or sparse vegetation, crop, grass, and shrub, the regional average C_h
301 values modeled by the C_{zil-h} run are the smallest in terms of three C_{zil} experiments. In
302 contrast, the default M-O scheme obtains overly high estimates, while the C_{zil-h}
303 simulations for forest are similar to the default run.

304 **3.2. Surface Energy and Water Variations Affected by C_{zil}**

305 The parameter C_h , representing the exchange efficiency between land and atmosphere,
306 plays an important role in controlling surface energy and water variables in the
307 Noah-MP LSM (Yang et al., 2011). The values of C_h simulated by the C_{zil-h} scheme
308 have been verified to be closer to the observations compared with the other two
309 schemes. Therefore, we further evaluated the potential skill of the three C_{zil} schemes
310 incorporated into the Noah-MP LSM in reproducing the observed surface energy and
311 water variables.

312 Figures 4–7 present the daily average soil temperature (ST) and SM at the depth of 0–
313 10 cm, as well as SH and LH, at nine ChinaFlux sites (Dan, Sw2, Cng, HaM, Du2,
314 Ha2, Qia, Din, and Cha; Table 1). The LSM shows the ability to favorably capture the
315 seasonal variability of the surface energy and water variables. For each C_{zil}
316 experiment, the simulations have significant correlations with the observations at the
317 nine sites, and the minimum correlation coefficients passing the 95% confidence level
318 for ST, SM, SH, and LH are 0.96 (Ha2), 0.38 (Cha), 0.32 (HaM), and 0.81 (Din),
319 respectively. All these results demonstrate that the Noah-MP LSM has good
320 performance with regard to the surface energy and water variables at these sites.
321 Comparisons of the simulated and observed ST at the nine stations are shown in
322 Figure 4 and Table 3. Generally, the values of ST are all underestimated by the three
323 C_{zil} schemes in comparison with the observations. However, the C_{zil-h} scheme
324 presents its superiority over the default M-O scheme and the $C_{zil} = 0.1$ scheme at most
325 sites. The C_{zil-h} scheme shows greater consistency between the simulation and the
326 observations, as revealed by the smallest RMSE at five of the nine sites (Dan, HaM,

327 Qia, Din, and Cha), as well as the highest correlation at six sites (Dan, Sw2, Du2, Qia,
328 Din, and Cha). The cold season ST values are substantially underestimated by all
329 three C_{zil} schemes, while the C_{zil-h} scheme slightly modulates the negative deviations.
330 The daily mean simulated SM values against the observations are shown in Figure 5
331 and Table 4. Precipitation is a key contributor to the seasonal variability of SM.
332 Usually, SM exhibits large daily variations during summer when most rainfall events
333 are concentrated, while SM fluctuations are stable during winter when fewer rainfall
334 events take place. The three C_{zil} schemes capture the seasonal evolutions of SM
335 reasonably well. There are dry biases at Sw2, Cng, HaM, and Cha, while the
336 remaining sites have wet biases. Similarly, the C_{zil-h} scheme slightly narrows the
337 discrepancy of the simulation from the observations, with the smallest RMSE at seven
338 of the nine sites. Figures 6 and 7 show daily averaged SH and LH variations,
339 respectively. Simulated SH shows positive biases against the observations for most
340 sites (Table 5), while LH shows negative values (Table 6). Compared with the other
341 two schemes, the C_{zil-h} scheme shows values of SH and LH that are more comparable
342 with the observations, with the smallest RMSE at most stations.

343 At the regional scale, we analyzed the seasonally spatial differences of LH and SH
344 modeled by the three C_{zil} experiments against FLUXNET-MTE observations, as
345 Figure 8 shows. Overall, the surface energy fluxes simulated with a dynamical
346 changing C_{zil} scheme show favorable spatial correspondence with FLUXNET-MTE
347 data. Moreover, it should also be noted that the influence of C_{zil} on LH is smaller
348 compared with SH, suggesting less spatial heterogeneity regarding the differences in
349 the modeling simulations.

350 **3.3. Impacts of C_{zil} on Short and Tall Canopy Types**

351 We have thus far shown that the variability of C_h across land cover types becomes
352 clear and that it can be divided roughly into short (grass, crop, and shrub) and tall
353 (forest) vegetation categories in order of increasing C_h . Therefore, from the

354 perspective of canopy types, we hereafter address the effect of C_{zil} on the simulations
355 in terms of on-site grassland (short canopy) and forest (tall canopy).

356 Synthetically considering the correlation coefficients and normalized standard
357 deviations (Figure 9), the C_{zil-h} experiments show that the majority of short vegetation
358 sites present significant improvements in the simulations, i.e., the C_{zil-h} simulations
359 closest to the observations occur at three of five sites (Sw2, HaM, and Du2) for LH, at
360 four sites (Dan, Sw2, Cng, and Du2) for SH, and at three sites (Dan, Cng, and HaM)
361 for SM. Regarding three tall vegetation sites (Qia, Din, and Cha), the C_{zil-h} scheme
362 shows the same level of ability as the default M-O in simulating the surface energy
363 and water components.

364 Diurnal surface heat fluxes for short and tall vegetation are shown in Figure 10. The
365 simulations for short vegetation are averages from five ChinaFlux grassland sites
366 (Dan, Sw2, Cng, HaM, and Du2), while those for tall vegetation are averages from
367 three forest sites (Qia, Din, and Cha). The modeled LH values show negligible
368 differences among the three C_{zil} schemes for both short and tall canopy types, but
369 underestimations (overestimations) are evident against the observed LH for short (tall)
370 canopy types. Comparatively, large discrepancies are found regarding the SH values
371 simulated by the different C_{zil} schemes, especially around midday (10:00–15:00 local
372 time). In comparison with the observed SH at grassland sites, the default M-O run
373 overestimates SH with coupling strength that is too strong, especially in summer;
374 however, the C_{zil-h} simulations agree well with the observed SH but with
375 underestimation in spring. For forest sites, the C_{zil-h} scheme produces the same level
376 of variation in SH as the default M-O scheme, while the $C_{zil} = 0.1$ scheme simulates
377 the smallest SH values.

378 **4. Discussions**

379 **4.1. Superiority of the C_{zil-h} Scheme in Regenerating Observations across Land**
380 **Cover Types**

381 The default M-O scheme substantially overestimates the land–atmosphere coupling
382 strength relative to the observations, which might illustrate a deficiency of LSMs, i.e.,
383 LSMs might have overly strong coupling that results in the transfer of too much
384 energy and water vapor (Chen & Zhang, 2009; Ruiz-Barradas & Nigam, 2005).
385 Correct determination of the coupling strength is closely related to the definition of
386 the calculation of Z_{ot} in LSMs (Brutsaert, 1982; Garratt, 1992; Sun & Mahrt, 1995).
387 The analysis in section 3 demonstrated that modest adjustment of the C_{zil} values
388 affecting the treatment of Z_{ot} in Eq. (5) could significantly improve the land–
389 atmosphere coupling strength. However, such impacts should be viewed across land
390 cover types. Compared with the default M-O scheme of the Noah-MP LSM, the C_{zil-h}
391 scheme provides significant improvements in the simulations for short vegetation;
392 improvements for tall canopy types are not evident, although the estimations are
393 reasonable, which is consistent with results obtained in North America (Chen et al.,
394 2019; Chen & Zhang, 2009). Regarding the ability for direct connection between
395 surface coupling strength and terrestrial ecosystems in Eq. (6), the C_{zil-h} scheme
396 realistically reduces the coupling strength for short canopy types, but produces
397 positive bias similar to that of the default M-O run for tall canopy types because of the
398 equivalent heat and momentum roughness length resulting from a close-to-zero C_{zil} .
399 Tall vegetation with a rough surface has large values of C_h , and hence generally
400 stronger coupling, with C_h values 10 times larger than for shorter vegetation (Chen &
401 Zhang, 2009). Regarding shorter canopy types, with increasing C_{zil} , the coupling
402 strength becomes weak, resulting in less rough surface for heat or moisture transfer,
403 and the simulated surface fluxes are less spatially heterogeneous. For the C_{zil-h}
404 scheme, the smaller values of C_{zil} resulting from the taller canopy enhance the C_h
405 values and hence the surface coupling strength; however, C_{zil} shows little change

406 when the canopy height is >5 m, as indicated by Eq. (6). For example, the difference
407 in C_{zil} values between vegetation canopy heights of 1 and 2 m is 0.24, whereas it is
408 only 1.51×10^{-8} between canopy heights of 19 and 20 m. As such, assigning different
409 C_{zil} values for different land cover types will allow the Noah-MP LSM to reasonably
410 reproduce the observed C_h . It should also be noted that the values of summer C_h are
411 slightly larger than spring because of the rougher surface with vegetation greening
412 from spring to summer. Therefore, in spring with the slightly weaker coupling
413 strength in comparison with summer, the C_{zil} - h scheme is likely to produce overly low
414 simulations, as shown in Figure 10a.

415 **4.2. Discrepancy of C_{zil} Impacts on Surface Energy Partitioning**

416 To understand how C_{zil} affects surface energy components, for instance, why the
417 influence of C_{zil} on LH appears smaller than on SH (Figure 10), we tried to account
418 for the issue from the perspective of the surface energy budget. Recent studies have
419 shown that the surface energy balance problem is subject to many factors, such as
420 measurement errors, heat storage in soil and canopy, as well as exchange processes on
421 large scales of the heterogeneous landscape (Etchevers et al., 2004; Foken, 2008;
422 Franssen et al., 2010; Tang et al., 2019). However, the available energy of net
423 radiation and ground heat flux as well as the turbulent fluxes of sensible and latent
424 heat are able to explain approximately 80% of the closure of the energy balance
425 (Kanemasu et al., 1992; Leuning et al., 1982; Wilson et al., 2002). Therefore, here, the
426 discrepancy of C_{zil} impacts on surface energy partitioning is considered in terms of
427 available energy and turbulent fluxes. Net radiation not directly provided by LSM
428 outputs can be derived as the residual of the radiation budget balance, i.e., the deficit
429 between downward and upward radiation (Xin et al., 2018). Figure 11 shows the
430 spatial relative differences between the C_{zil} schemes for SH, LH, ground heat flux, and
431 net radiation. The simulated SH and ground heat flux differ markedly with the C_{zil}
432 schemes, while the simulated net radiation appears insensitive to the C_{zil} values. For
433 LH, the values tend to vary little with the different C_{zil} schemes, but marked

434 differences can be found between the C_{zil-h} and default schemes in spring. The C_{zil-h}
435 experiment modeled smaller LH over eastern regions of China and larger values over
436 most western and northeastern areas. The situation was reversed for SH. The C_{zil-h}
437 scheme simulated smaller SH over much of China, leading to less heat being
438 transported from the surface into the atmosphere; thus, an increase in surface
439 temperature enhances ground heat flux.

440 **5. Conclusions**

441 The impact of land–atmosphere coupling within LSMs with regard to China has yet to
442 be clarified because of the complexity of climate change, terrain, and vegetation
443 distribution as well as the lack of observations. In this study, using observations
444 collected from nine ChinaFlux sites and data from over 2000 automatic
445 meteorological stations, the impacts of land–atmosphere coupling for different land
446 cover types over China were assessed. This was achieved by testing three C_{zil} schemes
447 (the default M-O, constant $C_{zil} = 0.1$, and dynamic canopy-height-dependent C_{zil-h}
448 schemes) with the offline Noah-MP LSM. The parameter C_{zil} is strongly associated
449 with C_h , which is a critical parameter in the transfer of surface energy into the lower
450 atmosphere and directly reflects the land–atmosphere coupling strength. By
451 performing both single-site and regional-scale experiments, we verified and compared
452 the sensibility of C_h and subsequently of the surface energy and water components in
453 response to different C_{zil} schemes. The main results of the study can be summarized as
454 follows.

455 The different C_{zil} schemes have considerable impact on surface coupling strength. The
456 default M-O scheme, which has equivalent roughness length for heat and momentum
457 with no- C_{zil} , substantially overestimates C_h . The constant $C_{zil} = 0.1$ scheme reduces
458 the positive C_h bias produced by the default scheme for short vegetation (grass, crop,
459 and shrub); however, it overly underestimates C_h for tall vegetation (forest). In
460 contrast, the C_{zil-h} scheme produces the least C_h bias against the observations for short

461 canopy types, and provides overestimated but reasonable values for tall canopy types,
462 similar to the default M-O simulation.

463 The accuracy of simulated surface water and energy components in LSMs is closely
464 related to surface coupling strength, which is in turn determined by C_{zil} . As the
465 discrepancies in C_h produced by the different C_{zil} schemes show, in general, the C_{zil-h}
466 scheme significantly reduces the bias against observations in comparison with the
467 default and constant C_{zil} schemes. The C_{zil-h} scheme can better reproduce the
468 observed surface energy components, while the improvement in water variables such
469 as SM remains limited.

470 Assigning different C_{zil} values for different land cover types displays the superiority
471 of the Noah-MP LSM in reproducing the observed C_h , as well as the surface variables
472 for short vegetation (grass, crop, and shrub), while the improvement for the tall
473 vegetation (forest) is not significant, although the estimation are reasonable. These
474 results underline the critical importance of C_{zil} in relation to canopy height in LSMs,
475 and thus raise other intriguing problems for further study, e.g., the question of how to
476 effectively improve simulations for tall vegetation through optimization of the C_{zil-h}
477 scheme, and how best to employ coupled climate models to investigate the effects of
478 C_h on climate simulations.

479

480

481 **Acknowledgments**

482 This work was funded by the National Key Research and Development Program of
483 China (grant number: 2016YFA0600403), National Natural Science Foundation of
484 China (grant number: 41875116), and Open fund of the Key Laboratory of Land
485 Surface Process and Climate Change in Cold Arid Area of the Chinese Academy of
486 Sciences “Influence of land–atmosphere coupling intensity on regional climate in arid
487 regions of Northwest China” (grant number: LPU2017001). The meteorological
488 station data used in this study are available from the China Meteorological

489 Administration (<http://data.cma.cn/>). The ChinaFlux observation data are from the
490 FLUXNET network (<http://www.fluxdata.org>), and the FLUXNET model tree
491 ensembles (MTE) latent heat flux and sensible heat flux data are from the Max Planck
492 Institute for Biogeochemistry (<http://www.bgc-jena.mpg.de/geodb/>). Model output
493 used is available at online (<https://doi.org/10.5281/zenodo.3560864>). There are no
494 conflicts of interest.

495

496

497 **References**

498 Barlage, M., Tewari, M., Chen, F., Miguez-Macho, G., Yang, Z. L., & Niu, G. Y.
499 (2015). The effect of groundwater interaction in North American regional climate
500 simulations with WRF/Noah-MP. *Climatic Change*, 129(3-4), 485-498.
501 doi:10.1007/s10584-014-1308-8.

502 Betts, A. K., Ball, J. H., Beljaars, A. C. M., Miller, M. J., & Viterbo, P. A. (1996).
503 The land surface-atmosphere interaction: A review based on observational and
504 global modeling perspectives. *Journal of Geophysical Research: Atmospheres*,
505 101(D3), 7209-7225. doi:10.1029/95jd02135.

506 Brovkin, V., Boysen, L., Raddatz, T., Gayler, V., Loew, A., & Claussen, M. (2013).
507 Evaluation of vegetation cover and land-surface albedo in MPI-ESM CMIP5
508 simulations. *Journal of Advances in Modeling Earth Systems*, 5(1), 48-57.
509 doi:10.1029/2012ms000169.

510 Brutsaert, W. A. (1982). *Evaporation into the atmosphere: Theory, history and*
511 *applications* (pp. 299). D. Reidel, Dordrecht, Netherlands: Cornell University,
512 USA. <https://doi.org/10.1007/978-94-017-1497-6>.

513 Cai, X. T., Yang, Z. L., David, C. H., Niu, G. Y., & Rodell, M. (2014). Hydrological
514 evaluation of the Noah-MP land surface model for the Mississippi River Basin.
515 *Journal of Geophysical Research-Atmospheres*, 119(1), 23-38.
516 doi:10.1002/2013jd020792.

517 Chen, F., & Dudhia, J. (2001). Coupling an advanced land surface-hydrology model
518 with the Penn State-NCAR MM5 modeling system. Part I: Model implementation
519 and sensitivity. *Monthly Weather Review*, 129(4), 569-585.
520 doi:10.1175/1520-0493(2001)129<0569:caalsh>2.0.co;2.

521 Chen, F., Janjic, Z., & Mitchell, K. (1997). Impact of atmospheric surface-layer
522 parameterizations in the new land-surface scheme of the NCEP mesoscale Eta
523 model. *Boundary-Layer Meteorology*, 85(3), 391-421.
524 doi:10.1023/a:1000531001463.

525 Chen, F., & Mitchell, K. (1999). Using the GEWEX/ISLSCP forcing data to simulate
526 global soil moisture fields and hydrological cycle for 1987-1988. *Journal of the*
527 *Meteorological Society of Japan*, 77(1B), 167-182.
528 doi:10.2151/jmsj1965.77.1B_167.

529 Chen, F., Mitchell, K., Schaake, J., Xue, Y. K., Pan, H. L., Koren, V., et al. (1996).
530 Modeling of land surface evaporation by four schemes and comparison with FIFE
531 observations. *Journal of Geophysical Research-Atmospheres*, 101(D3), 7251-7268.
532 doi:10.1029/95jd02165.

533 Chen, F., & Zhang, Y. (2009). On the coupling strength between the land surface and
534 the atmosphere: From viewpoint of surface exchange coefficients. *Geophysical*
535 *Research Letters*, 36(10), 1-5. doi:10.1029/2009gl037980.

536 Chen, L., Li, Y. P., Chen, F., Barlage, M., Zhang, Z., & Li, Z. H. (2019). Using 4-km
537 WRF CONUS simulations to assess impacts of the surface coupling strength on
538 regional climate simulation. *Climate Dynamics*, 53(9-10), 6397-6416.
539 doi:10.1007/s00382-019-04932-9.

540 Chen, L., Li, Y. P., Chen, F., Barr, A., Barlage, M., & Wan, B. C. (2016). The
541 incorporation of an organic soil layer in the Noah-MP land surface model and its
542 evaluation over a boreal aspen forest. *Atmospheric Chemistry and Physics*, 16(13),
543 8375-8387. doi:10.5194/acp-16-8375-2016.

544 Cosgrove, B. A., Lohmann, D., Mitchell, K. E., Houser, P. R., Wood, E. F., Schaake,
545 J. C., et al. (2003). Real-time and retrospective forcing in the North American
546 Land Data Assimilation System (NLDAS) project. *Journal of Geophysical*
547 *Research-Atmospheres*, 108(D22), 1-12. doi:10.1029/2002jd003118.

548 Dai, Y. J., Xin, Q. C., Wei, N., Zhang, Y. G., Wei, S. G., Yuan, H., et al. (2019). A
549 Global High-Resolution Data Set of Soil Hydraulic and Thermal Properties for
550 Land Surface Modeling. *Journal of Advances in Modeling Earth Systems*, 11(9),
551 2996-3023. doi:10.1029/2019ms001784.

552 Dirmeyer, P. A., Koster, R. D., & Guo, Z. C. (2006). Do global models properly
553 represent the feedback between land and atmosphere? *Journal of*
554 *Hydrometeorology*, 7(6), 1177-1198. doi:10.1175/jhm532.1.

555 Etchevers, P., Martin, E., Brown, R., Fierz, C., Lejeune, Y., Bazile, E., et al. (2004).
556 Validation of the energy budget of an alpine snowpack simulated by several snow
557 models (Snow MIP project). *Annals of Glaciology*, 38, 150–158.
558 <https://doi.org/10.3189/172756404781814825>

559 Foken, T. (2008). The energy balance closure problem: An overview. *Ecological*
560 *Applications*, 18(6), 1351-1367. doi:10.1890/06-0922.1.

561 Franssen, H. J. H., Stockli, R., Lehner, I., Rotenberg, E., & Seneviratne, S. I. (2010).
562 Energy balance closure of eddy-covariance data: A multisite analysis for European
563 FLUXNET stations. *Agricultural and Forest Meteorology*, 150(12), 1553-1567.
564 doi:10.1016/j.agrformet.2010.08.005.

565 Frydrychowicz-Jastrzebska, G., & Bugala, A. (2015). Modeling the Distribution of
566 Solar Radiation on a Two-Axis Tracking Plane for Photovoltaic Conversion.
567 *Energies*, 8(2), 1025-1041. doi:10.3390/en8021025.

568 Garratt, J. R. (1992). The atmospheric boundary layer (pp. 316). Cambridge
569 University Press, New York.

570 Gutmann, E. D., & Small, E. E. (2007). A comparison of land surface model soil
571 hydraulic properties estimated by inverse modeling and pedotransfer functions.
572 *Water Resources Research*, 43(5), 1-13. doi:10.1029/2006wr005135.

573 Jung, M., Reichstein, M., & Bondeau, A. (2009). Towards global empirical upscaling
574 of FLUXNET eddy covariance observations: validation of a model tree ensemble
575 approach using a biosphere model. *Biogeosciences*, 6(10), 2001-2013.
576 doi:10.5194/bg-6-2001-2009.

577 Kanemasu, E. T., Verma, S. B., Smith, E. A., Fritschen, L. J., Wesely, M., Field, R. T.,
578 et al. (1992). Surface flux measurements in FIFE: An overview. *Journal of*
579 *Geophysical Research-Atmospheres*, 97(D17), 18547-18555.
580 doi:10.1029/92jd00254.

581 Knist, S., Goergen, K., Buonomo, E., Christensen, O. B., Colette, A., Cardoso, R. M.,
582 et al. (2017). Land-atmosphere coupling in EURO-CORDEX evaluation
583 experiments. *Journal of Geophysical Research-Atmospheres*, 122(1), 79-103.
584 doi:10.1002/2016jd025476.

585 Koster, R. D., Dirmeyer, P. A., Guo, Z. C., Bonan, G., Chan, E., Cox, P., et al. (2004).
586 Regions of strong coupling between soil moisture and precipitation. *Science*,
587 305(5687), 1138-1140. doi:10.1126/science.1100217.

588 LeMone, M. A., Tewari, M., Chen, F., Alfieri, J. G., & Niyogi, D. (2008). Evaluation
589 of the Noah Land Surface Model Using Data from a Fair-Weather IHOP_2002
590 Day with Heterogeneous Surface Fluxes. *Monthly Weather Review*, 136(12),
591 4915-4941. doi:10.1175/2008mwr2354.1.

592 Leuning, R., Denmead, O. T., Lang, A. R. G., & Ohtaki, E. (1982). Effects of heat and
593 water-vapor transport on eddy covariance measurement of co2 fluxes.
594 *Boundary-Layer Meteorology*, 23(2), 209-222. doi:10.1007/bf00123298.

595 Li, Z., Liu, W. Z., Zhang, X. C., & Zheng, F. L. (2009). Impacts of land use change
596 and climate variability on hydrology in an agricultural catchment on the Loess

597 Plateau of China. *Journal of Hydrology*, 377(1-2), 35-42.
 598 doi:10.1016/j.jhydrol.2009.08.007.

599 Liu, C. H., Ikeda, K., Rasmussen, R., Barlage, M., Newman, A. J., Prein, A. F., et al.
 600 (2017). Continental-scale convection-permitting modeling of the current and
 601 future climate of North America. *Climate Dynamics*, 49(1-2), 71-95.
 602 doi:10.1007/s00382-016-3327-9.

603 Los, S. O., Weedon, G. P., North, P. R. J., Kaduk, J. D., Taylor, C. M., & Cox, P. M.
 604 (2006). An observation-based estimate of the strength of rainfall-vegetation
 605 interactions in the Sahel. *Geophysical Research Letters*, 33(16), 5.
 606 doi:10.1029/2006gl027065.

607 Mahmood, R., & Hubbard, K. G. (2003). Simulating sensitivity of soil moisture and
 608 evapotranspiration under heterogeneous soils and land uses. *Journal of Hydrology*,
 609 280(1-4), 72-90. doi:10.1016/s0022-1694(03)00183-5.

610 Moncrieff, M. W. (2004). Analytic representation of the large-scale organization of
 611 tropical convection. *Journal of the Atmospheric Sciences*, 61(13), 1521-1538.
 612 doi:10.1175/1520-0469(2004)061<1521:arotlo>2.0.co;2.

613 Niu, G. Y., Yang, Z. L., Mitchell, K. E., Chen, F., Ek, M. B., Barlage, M., et al.
 614 (2011). The community Noah land surface model with multiparameterization
 615 options (Noah-MP): 1. Model description and evaluation with local-scale
 616 measurements. *Journal of Geophysical Research-Atmospheres*, 116, 1-19.
 617 doi:10.1029/2010jd015139.

618 Pilotto, I. L., Rodriguez, D. A., Tomasella, J., Sampaio, G., & Chou, S. C. (2015).
 619 Comparisons of the Noah-MP land surface model simulations with measurements
 620 of forest and crop sites in Amazonia. *Meteorology and Atmospheric Physics*,
 621 127(6), 711-723. doi:10.1007/s00703-015-0399-8.

622 Rodell, M., Houser, P. R., Jambor, U., Gottschalck, J., Mitchell, K., Meng, C. J., et al.
 623 (2004). The global land data assimilation system. *Bulletin of the American*
 624 *Meteorological Society*, 85(3), 381-+. doi:10.1175/bams-85-3-381.

625 Ruiz-Barradas, A., & Nigam, S. (2005). Warm season rainfall variability over the US
626 great plains in observations, NCEP and ERA-40 reanalyses, and NCAR and
627 NASA atmospheric model simulations. *Journal of Climate*, 18(11), 1808-1830.
628 doi:10.1175/jcli3343.1.

629 Santanello, J. A., Peters-Lidard, C. D., Kumar, S. V., Alonge, C., & Tao, W. K.
630 (2009). A Modeling and Observational Framework for Diagnosing Local
631 Land-Atmosphere Coupling on Diurnal Time Scales. *Journal of*
632 *Hydrometeorology*, 10(3), 577-599. doi:10.1175/2009jhm1066.1.

633 Skamarock, W.C., Klemp, J. B., Dudhia, J., Gill, D. O., Barker, D. M., Duda, M. G.,
634 et al. (2008). A description of the Advanced ResearchWRF version 3. NCAR
635 Technical Notes, NCAR/TN - 4751STR.

636 Sun, J. L., & Mahrt, L. (1995). Determination of surface fluxes from the surface
637 radiative temperature. *Journal of the Atmospheric Sciences*, 52(8), 1096-1106.
638 doi:10.1175/1520-0469(1995)052<1096:dosfft>2.0.co;2.

639 Tang, S. Q., Xie, S. C., Zhang, M. H., Tang, Q., Zhang, Y. Y., Klein, S. A., et al.
640 (2019). Differences in Eddy-Correlation and Energy-Balance Surface Turbulent
641 Heat Flux Measurements and Their Impacts on the Large-Scale Forcing Fields at
642 the ARM SGP Site. *Journal of Geophysical Research-Atmospheres*, 124(6),
643 3301-3318. doi:10.1029/2018jd029689.

644 Trier, S. B., LeMone, M. A., Chen, F., & Manning, K. W. (2011). Effects of Surface
645 Heat and Moisture Exchange on ARW-WRF Warm-Season Precipitation
646 Forecasts over the Central United States. *Weather and Forecasting*, 26(1), 3-25.
647 doi:10.1175/2010waf2222426.1.

648 Wilson, K., Goldstein, A., Falge, E., Aubinet, M., Baldocchi, D., Berbigier, P., et al.
649 (2002). Energy balance closure at FLUXNET sites. *Agricultural and Forest*
650 *Meteorology*, 113(1-4), 223-243. doi:10.1016/s0168-1923(02)00109-0.

651 Xin, Y. F., Chen, F., Zhao, P., Barlage, M., Blanken, P., Chen, Y. L., et al. (2018).
652 Surface energy balance closure at ten sites over the Tibetan plateau. *Agricultural*
653 *and Forest Meteorology*, 259, 317-328. doi:10.1016/j.agrformet.2018.05.007.

654 Yang, K., Koike, T., Ishikawa, H., Kim, J., Li, X., Liu, H. Z., et al. (2008). Turbulent
655 flux transfer over bare-soil surfaces: Characteristics and parameterization. *Journal*
656 *of Applied Meteorology and Climatology*, 47(1), 276-290.
657 doi:10.1175/2007jamc1547.1.

658 Yang, Z. L., Dickinson, R. E., Henderson-Sellers, A., & Pitman, A. J. (1995).
659 Preliminary-study of spin-up processes in land-surface models with the first stage
660 data of project for intercomparison of land-surface parameterization schemes
661 phase 1(a). *Journal of Geophysical Research-Atmospheres*, 100(D8), 16553-16578.
662 doi:10.1029/95jd01076.

663 Yang, Z. L., Niu, G. Y., Mitchell, K. E., Chen, F., Ek, M. B., Barlage, M., et al.
664 (2011). The community Noah land surface model with multiparameterization
665 options (Noah-MP): 2. Evaluation over global river basins. *Journal of Geophysical*
666 *Research-Atmospheres*, 116, 1-16. doi:10.1029/2010jd015140.

667 Zhang, J. Y., Wang, W. C., & Leung, L. R. (2008). Contribution of land-atmosphere
668 coupling to summer climate variability over the contiguous United States. *Journal*
669 *of Geophysical Research-Atmospheres*, 113, 1-15. doi:10.1029/2008jd010136.

670 Zheng, Y., Kumar, A., & Niyogi, D. (2015). Impacts of land-atmosphere coupling on
671 regional rainfall and convection. *Climate Dynamics*, 44(9-10), 2383-2409.
672 doi:10.1007/s00382-014-2442-8.

673 Zilitinkevich, S. S. (1995). Non-local turbulent transport: Pollution dispersion aspects
674 of coherent structure of convective flows. In H. Power, N. Moussiopoulos, & C. A.
675 Brebbia (Eds.), *Air pollution III-volume I. Air pollution theory and simulation* (pp.
676 53–60). Southampton, Boston: Computational Mechanics Publications.

677
678

679

680

681 **Table 1.** General information regarding the nine FLUXNET sites.

Site Code	Site Name	Latitude, Longitude	Elevation (m)	Land-Cover Type	Canopy Height (m)	Years
CN-Dan	Dangxiong	30.50, 91.07	4250	GRA	0.1	2004-2005
CN-Sw2	Siziwang Banner	41.79, 111.90	1456	GRA	0.1~0.2	2011
CN-Cng	Changling	44.59, 123.51	270	GRA	0.17	2008
CN-HaM	Haibei Alpine	37.37, 101.18	3190	GRA	0.25	2003
CN-Du2	Duolun	42.05, 116.28	1324	GRA	0.3	2007
CN-Ha2	Haibei Shrubland	37.61, 101.33	3190	WET	0.6–0.7	2003-2005
CN-Qia	Qianyanzhou	26.74, 115.06	100	ENF	12	2003-2005
CN-Din	Dinghushan	23.17, 112.54	240	EBF	17	2003-2005
CN-Cha	Changbaishan	42.40, 128.10	738	MF	26	2003-2005

682 GRA: grasslands; WET: permanent wetlands; ENF: evergreen needleleaf forest; EBF: evergreen broadleaf forest;
683 MF: mixed forests

684

685

686

687

688

689

690

691

692

693

694

695

696

697

698

699

700

701

702

703

704

705

706 **Table 2.** Noah-MP LSM parameterization options used in this study.

Parameterization description	Options
Dynamic vegetation	4: table LAI, shdfac=maximum
Stomatal resistance	1: BALL-Berry (Ball et al., 1987)
Soil moisture factor for stomatal resistance	1: original Noah (Chen and Dudhia, 2001)
Runoff/soil lower boundary	1: original surface and subsurface runoff (free drainage)
Surface layer drag coefficient calculation	1: Monin–Obukhov (Brutsaert, 1982)
Supercooled liquid water	1: no iteration (Niu and Yang, 2006)
Soil permeability	1: linear effects, more permeable (Niu and Yang, 2006)
Radiative transfer	3: two-stream applied to vegetated fraction
Surface albedo	2: CLASS (Verseghy, 1991)
Precipitation partitioning between snow and rain	1: Jordan (Jordan, 1991)
Soil temp lower boundary	2: TBOT at ZBOT (8 m) read from a file
Snow/soil temperature time	1: semi-implicit

707

708

709

710

711

712

713

714

715

716

717

718

719

720

721

722

723

724
725
726

727 **Table 3.** Statistics of daily averaged soil temperature at the depth of 0–10 cm from the
728 nine FLUXNET sites. R, MBE, and RMSE denote the Pearson correlation coefficient,
729 mean bias error, and root mean square error between the observation and simulation,
730 respectively. Soil temperature simulated by the Noah-MP LSM using the default M-O
731 scheme is represented by Default; using the $C_{zil} = 0.1$ scheme is represented by Czil;
732 and using the C_{zil-h} scheme is represented by Newczil.

Site Code	Default			Czil			Newczil		
	R	MBE	RMSE	R	MBE	RMSE	R	MBE	RMSE
CN-Dan	0.98	-0.97	2.90	0.98	0.66	2.42	0.98	0.66	2.42
CN-Sw2	0.99	-3.47	21.30	0.99	-3.65	22.79	0.99	-3.44	23.90
CN-Cng	0.99	0.62	14.34	0.98	0.61	14.94	0.98	1.11	19.20
CN-HaM	0.97	-4.81	29.42	0.97	-4.66	28.32	0.97	-4.01	25.82
CN-Du2	0.99	-1.93	7.58	0.99	-1.80	7.39	0.99	-1.17	7.68
CN-Ha2	0.97	-2.54	10.89	0.97	-1.97	10.45	0.96	-1.07	16.29
CN-Qia	0.99	-0.47	3.22	0.99	0.46	4.39	0.99	-0.47	3.22
CN-Din	0.97	-0.09	2.99	0.97	0.70	3.67	0.97	-0.09	2.99
CN-Cha	0.97	-0.81	17.25	0.97	-0.22	21.12	0.97	-0.81	17.25

733
734
735
736
737
738
739
740
741
742
743
744
745
746
747
748
749

750
751
752

753 **Table 4.** As in Table 3 but for soil moisture at the depth of 0–10 cm.

Site Code	Default			Czil			Newczil		
	R	MBE	RMSE	R	MBE	RMSE	R	MBE	RMSE
CN-Dan	0.84	0.07	0.01	0.87	0.07	0.01	0.87	0.07	0.01
CN-Sw2	0.72	-0.01	0.002	0.72	-0.01	0.002	0.69	-0.01	0.002
CN-Cng	0.69	-0.13	0.04	0.69	-0.13	0.04	0.72	-0.13	0.04
CN-HaM	0.94	-0.13	0.02	0.94	-0.13	0.02	0.95	-0.13	0.02
CN-Du2	0.70	0.03	0.003	0.71	0.03	0.003	0.73	0.02	0.002
CN-Ha2	0.87	0.05	0.01	0.86	0.05	0.01	0.83	0.05	0.01
CN-Qia	0.54	0.16	0.03	0.55	0.16	0.03	0.54	0.16	0.03
CN-Din	0.77	0.04	0.003	0.76	0.04	0.003	0.77	0.04	0.003
CN-Cha	0.38	-0.08	0.02	0.39	-0.09	0.02	0.38	-0.08	0.02

754
755
756
757
758
759
760
761
762
763
764
765
766
767
768
769
770
771
772
773
774
775

776
777
778
779
780

781 **Table 5.** As in Table 3 but for sensible heat flux.

Site Code	Default			Czil			Newczil		
	R	MBE	RMSE	R	MBE	RMSE	R	MBE	RMSE
CN-Dan	0.54	12.25	663.28	0.54	4.66	340.11	0.54	4.66	340.11
CN-Sw2	0.82	-9.37	508.41	0.83	-9.19	468.04	0.85	-12.21	424.84
CN-Cng	0.74	7.29	442.85	0.75	6.45	387.70	0.73	2.66	274.10
CN-HaM	0.32	-12.03	679.30	0.33	-12.69	597.83	0.33	-13.29	462.76
CN-Du2	0.74	2.57	602.27	0.75	0.87	529.45	0.75	-5.22	461.64
CN-Ha2	0.51	-10.54	905.12	0.56	-13.32	765.79	0.57	-19.20	769.01
CN-Qia	0.73	10.07	391.62	0.70	3.61	242.20	0.73	10.07	391.57
CN-Din	0.65	3.36	213.55	0.57	-2.43	228.10	0.65	3.36	213.55
CN-Cha	0.69	16.06	677.90	0.73	8.56	377.00	0.69	16.06	677.90

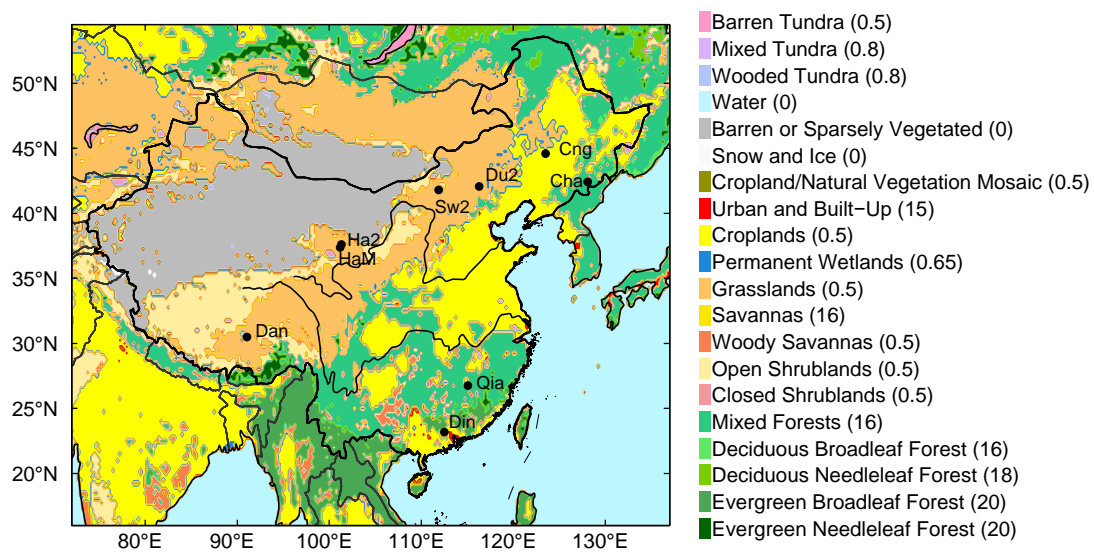
782
783
784
785
786
787
788
789
790
791
792
793
794
795
796
797
798
799
800
801

802
803
804
805
806

807 **Table 6.** As in Table 3 but for latent heat flux.

Site Code	Default			Czil			Newczil		
	R	MBE	RMSE	R	MBE	RMSE	R	MBE	RMSE
CN-Dan	0.90	-15.16	770.62	0.92	-14.87	732.86	0.92	-14.87	732.86
CN-Sw2	0.83	-9.63	232.85	0.83	-9.68	233.76	0.83	-9.61	231.80
CN-Cng	0.90	-5.65	212.66	0.91	-5.65	205.26	0.92	-5.74	173.62
CN-HaM	0.93	3.44	169.75	0.93	3.70	169.13	0.93	1.89	121.43
CN-Du2	0.82	-5.54	167.17	0.82	-5.39	163.21	0.83	-5.14	163.64
CN-Ha2	0.90	-10.03	378.07	0.91	-9.08	329.46	0.93	-9.09	282.24
CN-Qia	0.87	5.03	368.81	0.86	4.45	383.47	0.87	5.03	368.83
CN-Din	0.81	6.36	564.07	0.82	6.82	496.01	0.81	6.36	564.06
CN-Cha	0.94	-4.36	144.94	0.94	-1.94	134.29	0.94	-4.36	144.94

808
809
810
811
812
813
814
815
816
817
818
819
820



821

822 **Figure 1.** Noah-MP modeling domain and the locations of the nine ChinaFlux sites
 823 (dark circles). Shaded contours represent IGBP/MODIS land cover/land use
 824 classification. Values in parentheses indicate canopy height (unit: m).

825

826

827

828

829

830

831

832

833

834

835

836

837

838

839

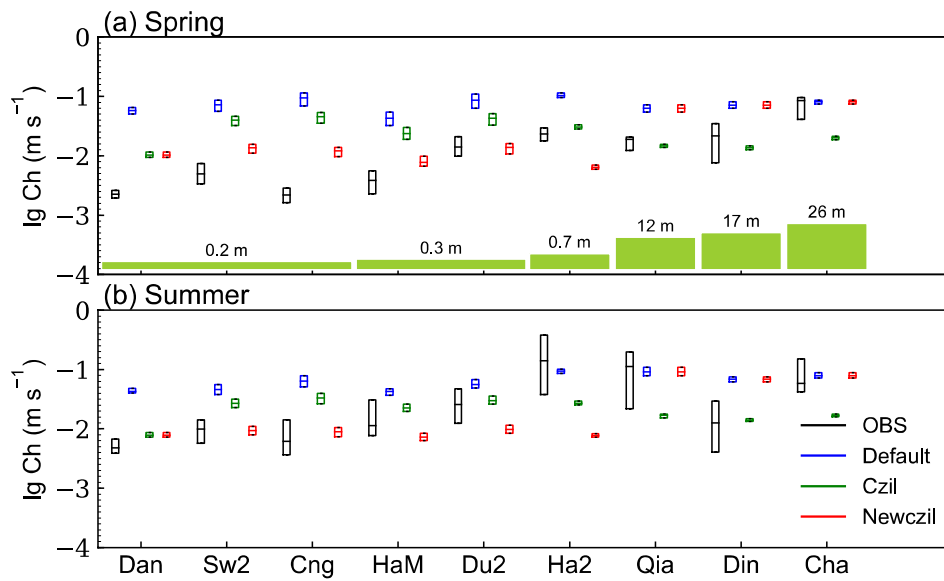
840

841

842

843

844



845

846 **Figure 2.** C_h (plotted at log10 scale) derived from the ChinaFlux observations, and
 847 calculated by the Noah-MP LSM using the default M-O, $C_{zil} = 0.1$, and C_{zil-h} schemes.
 848 These are midday (10:00–15:00 local time) values and averaged for (a) spring and (b)
 849 summer. Each box comprises 75% of all midday C_h values for every site, while the
 850 middle lines represent the median values of spring (summer) average C_h . Green bars
 851 in (a) denote canopy height for each site. Observations are represented by OBS; C_h
 852 calculated by the Noah-MP LSM using the default M-O scheme is represented by
 853 Default; using the $C_{zil} = 0.1$ scheme is represented by Czil; and using the C_{zil-h}
 854 scheme is represented by Newczil.

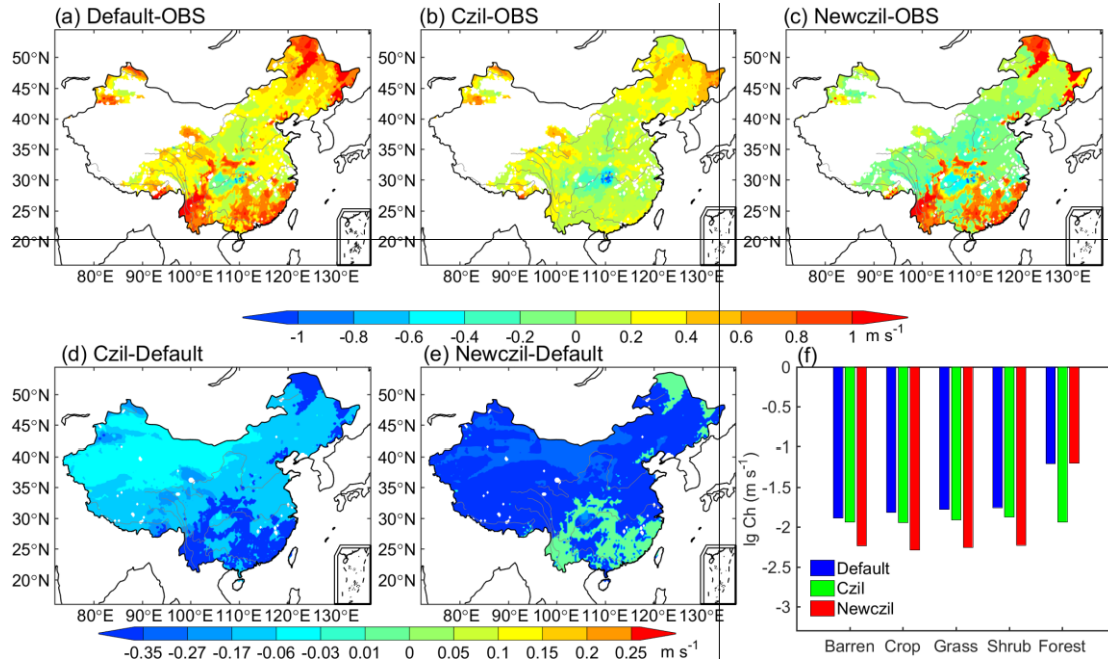
855

856

857

858

859



860

861 **Figure 3.** Comparisons of C_h (plotted at log10 scale) over China derived from on-site
 862 observations, and calculated by the Noah-MP LSM using the default M-O, $C_{zil} = 0.1$,
 863 and C_{zil-h} schemes during the summers of 2003–2012. The differences between the
 864 observations and the values simulated by the three schemes are shown in (a)–(c), and
 865 the differences between both the $C_{zil} = 0.1$ and the C_{zil-h} schemes and the default M-O
 866 scheme are shown in (d) and (e), respectively. Regional averaged C_h values for typical
 867 land cover types are shown in (f). The C_h values in (d)–(f) are midday (average of
 868 09:00, 12:00, and 15:00 local time) averages, but those in (a)–(c) are daily averages
 869 because only daily observations were available.

870

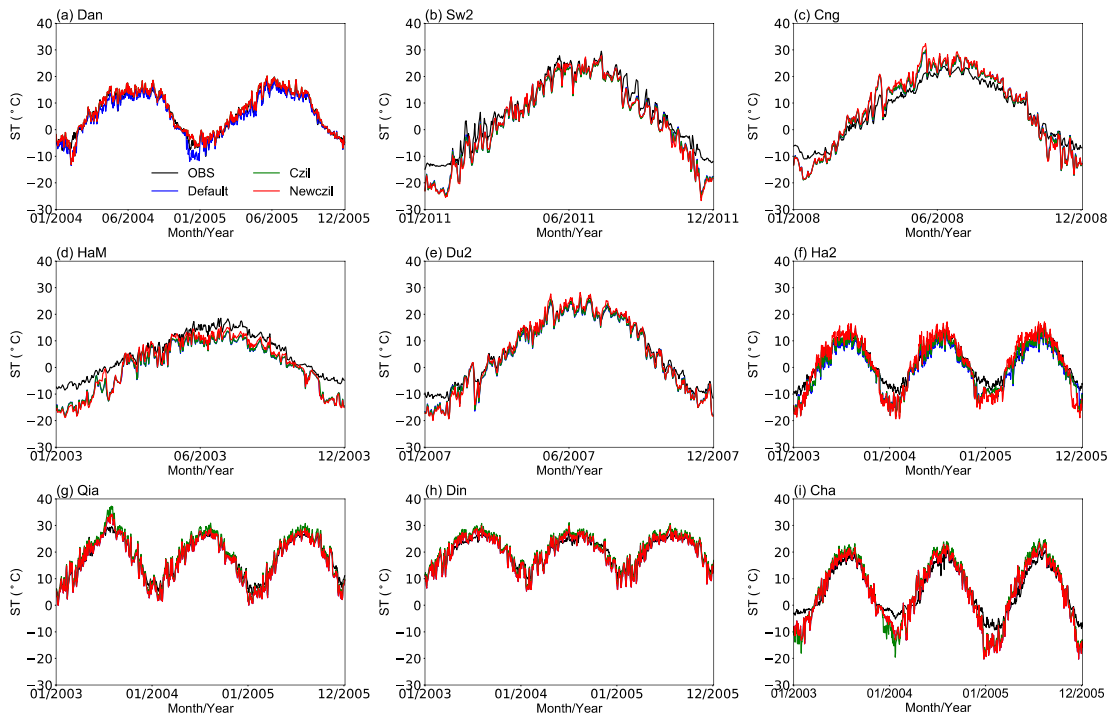
871

872

873

874

875



876

877 **Figure 4.** Comparisons of daily average soil temperature (ST) at the depth of 0–10 cm
 878 between the ChinaFlux observations and the Noah-MP LSM simulations using the
 879 default M-O, $C_{zil} = 0.1$, and C_{zil-h} schemes.

880

881

882

883

884

885

886

887

888

889

890

891

892

893

894

895

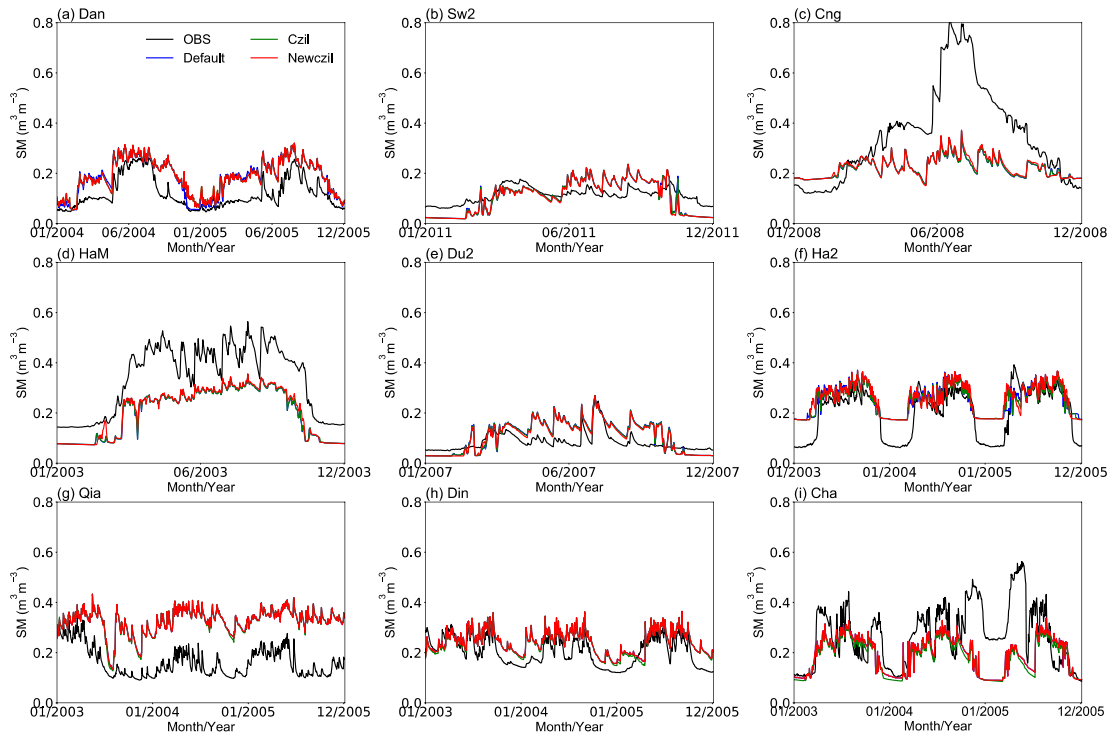
896

897

898

899

900



901

902 **Figure 5.** As in Figure 4 but for soil moisture (SM) at the depth of 0–10 cm.

903

904

905

906

907

908

909

910

911

912

913

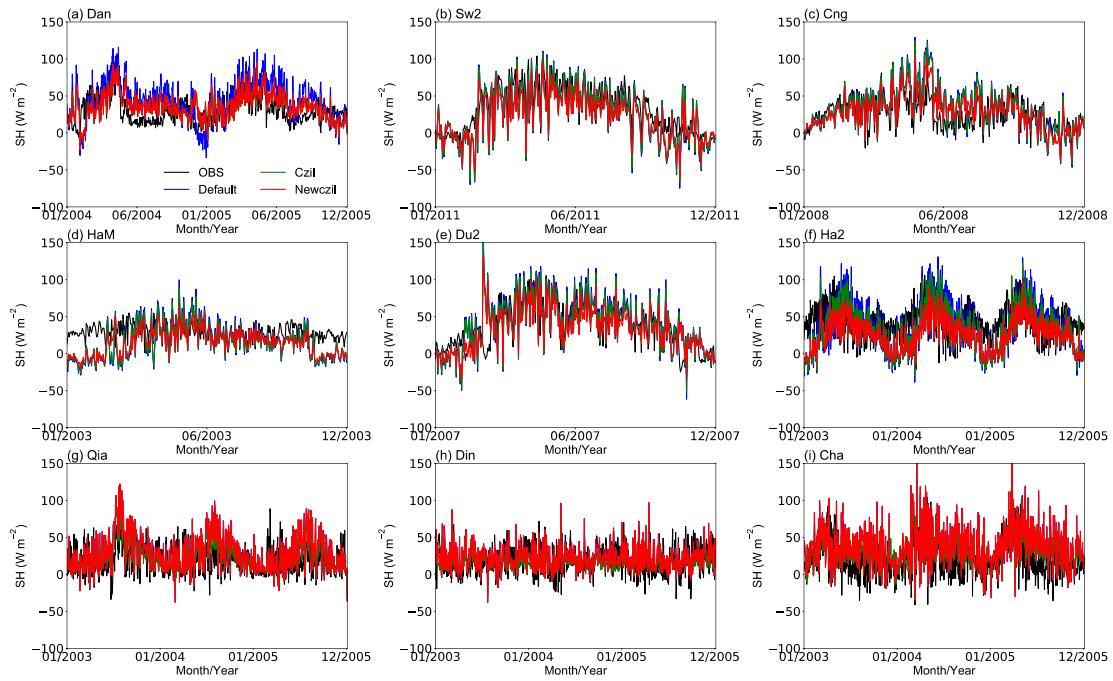
914

915

916

917

918



919

920 **Figure 6.** As in Figure 4 but for sensible heat flux (SH).

921

922

923

924

925

926

927

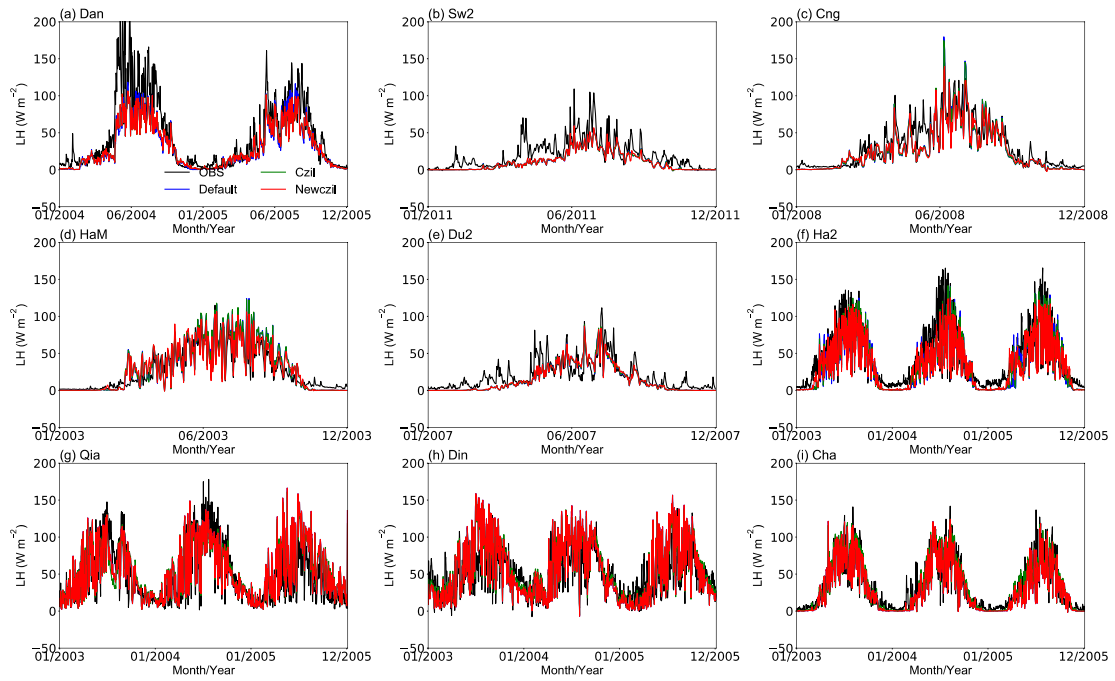
928

929

930

931

932



933

934 **Figure 7.** As in Figure 4 but for latent heat flux (LH).

935

936

937

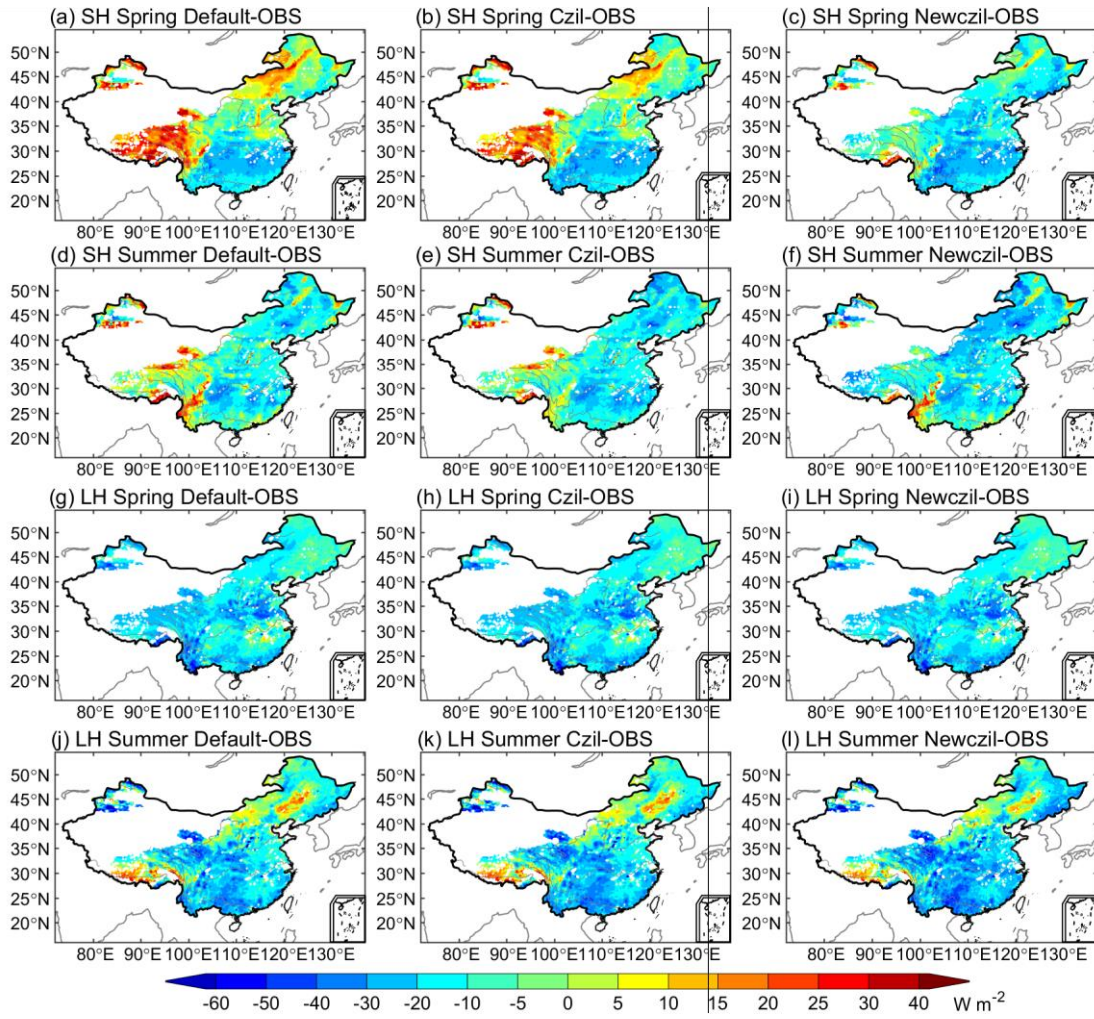
938

939

940

941

942



943

944 **Figure 8.** Seasonally spatial differences of LH and SH simulated by the Noah-MP LSM
 945 using the default M-O, $C_{zil} = 0.1$, and C_{zil-h} schemes against FLUXNET-MTE
 946 observations during spring and summer 2003–2012.

947

948

949

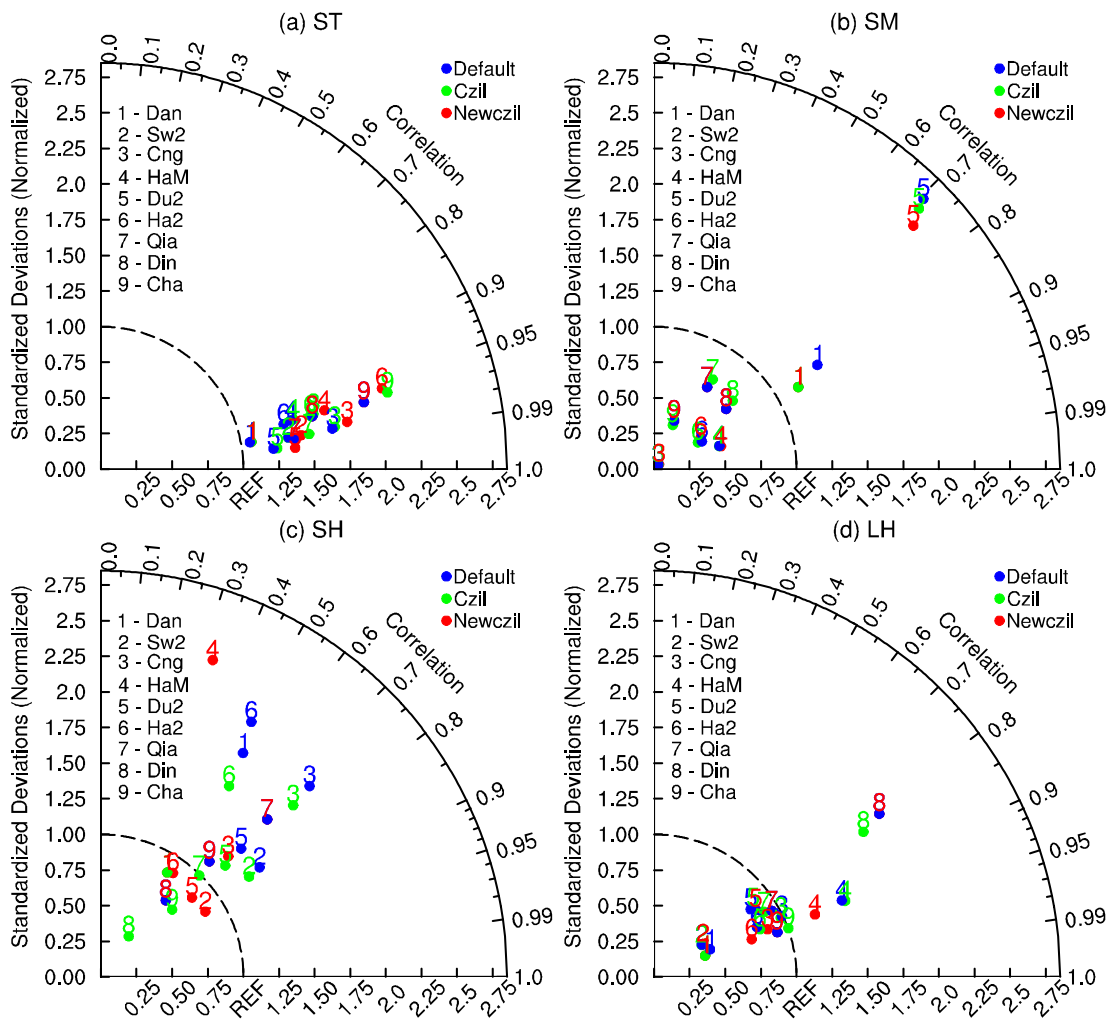
950

951

952

953

954



955

956 **Figure 9.** Statistics of daily averaged ST, SM, SH, and LH between the ChinaFlux
 957 observations and the Noah-MP LSM simulations using the default M-O, $C_{zil} = 0.1$, and
 958 C_{zil-h} schemes. SM and ST are at the depth of 0–10 cm.

959

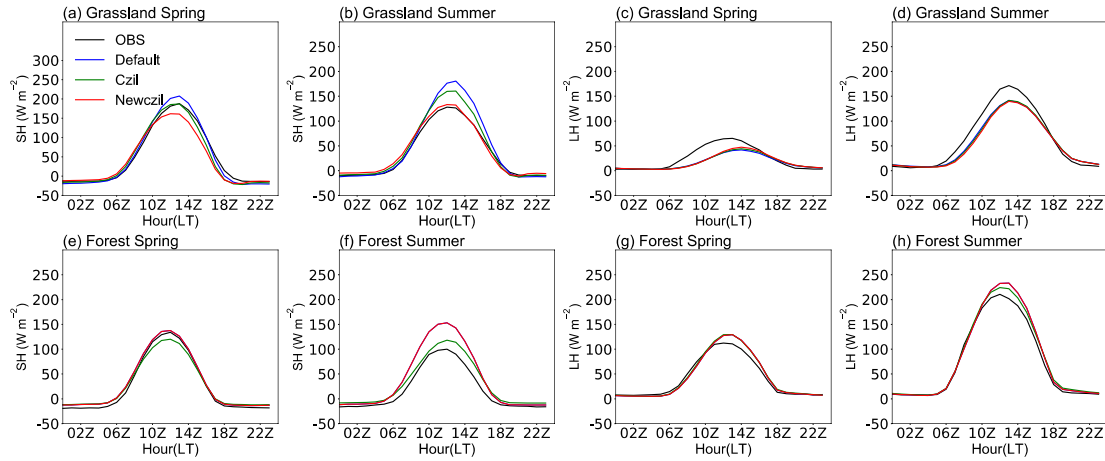
960

961

962

963

964



965

966 **Figure 10.** Comparisons of SH and LH between the ChinaFlux observations and the
 967 Noah-MP LSM simulations using the default M-O, $C_{zil} = 0.1$, and C_{zil-h} schemes for
 968 short and tall vegetation types. The values in (a)–(d) represent short vegetation types
 969 averaged from five ChinaFlux grassland sites (Dan, Sw2, Cng, HaM, and Du2), and
 970 those in (e)–(h) represent tall vegetation types averaged from three ChinaFlux forest
 971 sites (Qia, Din, and Cha).

972

973

974

975

976

977

978

979

980

981

982

983

984

985

986

987

988

989

990

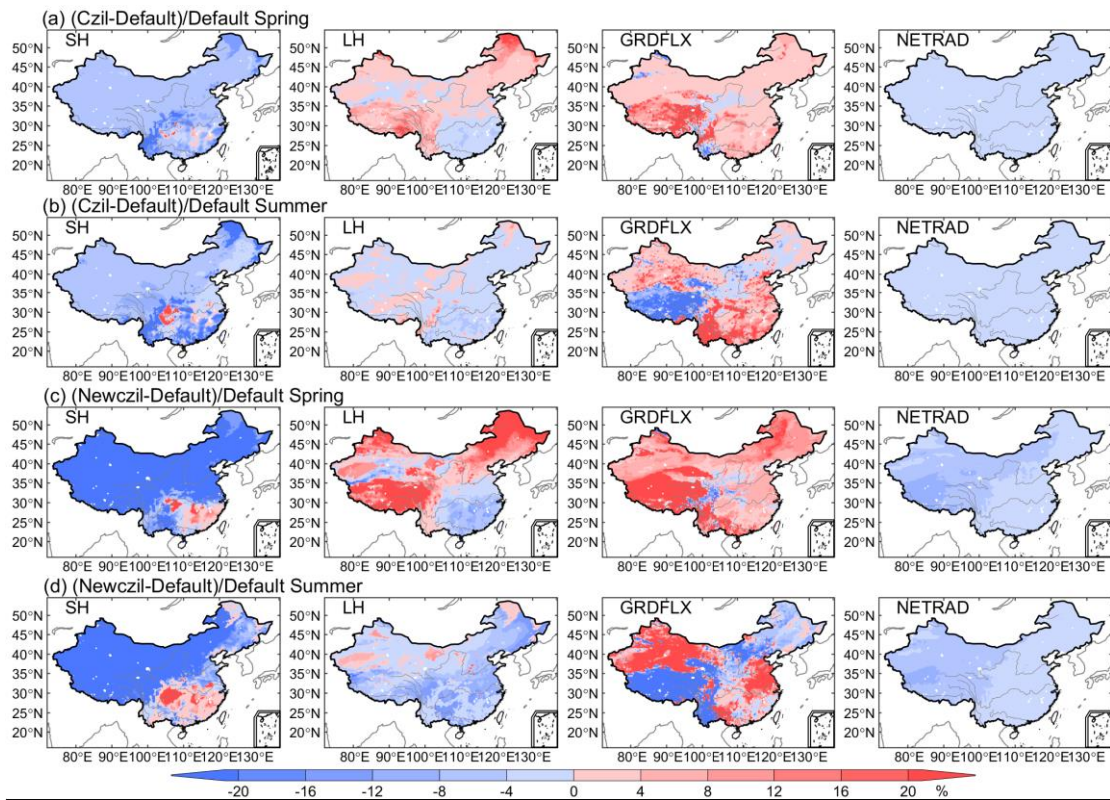
991

992

993

994

995



998 **Figure 11.** Spatial difference patterns of SH, LH, ground heat flux (GRDFLX), and net
 999 radiation (NETRAD) between the $C_{zil} = 0.1$ and default M-O schemes during spring
 1000 and summer 2003–2012 are shown in (a) and (b), and the difference patterns between
 1001 the $C_{zil}-h$ and default M-O schemes are shown in (c) and (d).

1002
 1003
 1004
 1005
 1006
 1007
 1008
 1009
 1010
 1011
 1012
 1013
 1014
 1015
 1016